PHYSICAL REVIEW E **66**, 051504 (2002)

Rotation due to hydrodynamic interactions between two spheres in contact

M. L. Ekiel-Jeżewska,[1,*] N. Lecoq,[2] R. Anthore,[2] F. Bostel,[2] and F. Feuillebois[3]
[1]*Institute of Fundamental Technological Research, Polish Academy of Sciences, Świętokrzyska 21, 00-049 Warsaw, Poland*
[2]*Université de Rouen, UMR 6634 CNRS, 76821 Mont Saint Aignan Cédex, France*
[3]*Physique Thermique, PMMH, École Supérieure de Physique et de Chimie Industrielles,*
10 rue Vauquelin, 75231 Paris Cédex 05, France

(Received 15 April 2002; published 26 November 2002)

We analyze the rotational and translational motion of two close spheres in a fluid at low Reynolds number to investigate if their surfaces come into mechanical contact. The rotational motion of a sphere settling close to another fixed ball is calculated from a model in which contact interactions between the spheres are added to the gravitational and hydrodynamic forces. The model predicts a transition from pure rolling to rolling with slip, determined by the Coulomb's law, when the ratio of the mechanical friction to the load increases up to the static friction coefficient. The dependence of the angular and translational velocities on the kinetic friction coefficient and on the separation between the particle surfaces is analyzed. The angular and translational velocities of a millimeter size bead in a viscous oil, close to a fixed bead of a similar size, are measured from video images. Interferometric data on translational motion are also collected according to the method introduced in our earlier studies. A systematic fitting procedure of the model to the experiment is developed and applied to the rotational and translational measurements. The model parameters are determined.

DOI: 10.1103/PhysRevE.66.051504 PACS number(s): 47.15.Gf, 47.15.Pn, 46.55.+d, 81.40.Pq

I. INTRODUCTION

The understanding and calculation of the macroscopic structure and transport properties of suspensions, such as the effective viscosity or the sedimentation velocity, are based on the investigation of hydrodynamic interactions between the suspension particles immersed in a fluid [1–9]. One of very special, inherent features of such interactions is that the so-called lubrication forces between close particle surfaces separated by a thin liquid layer increase indefinitely with the decrease of the gap size [10]. The fluid between two smooth rigid spheres resists their approach so strongly that it prevents both surfaces from touching each other. However, the real particles have certain asperities, and the question whether (and under which conditions) they actually get into contact is a subject of recent studies [11–17].

The practical reason for such investigations is that the contribution from very close distances between pairs of particles gives a non-negligible contribution to the macroscopic properties of suspensions, even if they are not dense [18–22]. As a result, the existence of contact interactions between rough particle surfaces is expected to simplify the calculations and to influence the suspension structure and values of its transport coefficients [23]. Quantitative estimations of such modifications [13,24–28] are based on very simple models of the contact. For example, in the simplest stick-rotate model, both particles are locked together [29–31]. The alternative roll-slip model [13,15], which we use in this paper, assumes that for very close spheres mechanical friction forces should be added to the other forces acting on the particles (i.e., hydrodynamic, gravitational, etc.). Then the description of the mechanical friction forces is based on the standard friction theory [32–34]. The model predicts two regions of the motion: pure rolling and rolling with slip described by the standard Coulomb's law. The roll-slip model deals with averaged quantities such as an effective distance between the particle surfaces rather than with the local real separation, which varies with time [17].

Before applying a model of contact to describe a suspension, it is essential to study in detail how the contact interactions modify the two-particle relative translational and rotational motion, and verify these predictions in corresponding experiments. For example, the measurements of the relative translational velocities of two particles in a fluid at rest from Ref. [14], are neither in agreement with the stick-rotate model, nor with the roll-without-slip model, nor with the frictionless roll-slip model [14].

Descriptions of the two systems of touching spheres within the roll-slip model were constructed [13,15] and shown to be in agreement with the measurements of the particle *translational* velocities [14,15]. In Ref. [15] one sphere was fixed, and the other one was moving due to gravity; in Refs. [13,14] both spheres were mobile—one was heavy and the other one was buoyant. The translational motion of spheres was measured by a video technique in Ref. [14] and by an interferometric method [35,36] in Refs. [15,37].

However, the fitting of the experimental data performed in these approaches leads only to rough estimates of the model parameters. There exist three reasons for this drawback. First, there exists an essential theoretical source of the inaccuracy; that is, the lubrication forces depend logarithmically on the gap size and this is why the motion is weakly sensitive to changes of the effective averaged distance between the particle surfaces. Second, the model depends on four parameters, and it is difficult to evaluate their values and uncertainty by a simultaneous fit of them all. Third, during the rolling with slip, there appear large velocity fluctuations which do not allow to benefit from the high accuracy of interferometry. As a result, measurements of the relative

---

[*] Electronic address: mekiel@ippt.gov.pl

translational velocities practically do not allow to specify what is the effective distance between the particle surfaces [15].

To remove this inaccuracy, in this paper we analyze both theoretically and experimentally the relative *rotational* motion of two close spheres, in addition to the translational one [38]. We develop a systematic procedure to compare the model of combined contact and hydrodynamic interactions with the experimental results for the relative translational and rotational motion of two close spheres and we discuss how it improves in accuracy over the previous studies of the translation only.

In Sec. II we derive the model equations for the rotation and combine them with the formulas for the translation [15]. In Sec. III we present the experiment and describe our analysis of the video images and their coupling with the interferometric measurements. In Sec. IV we select the variables to be compared with the experiment in order to optimize the accuracy, and we calculate from the model their time dependence. In Sec. V we present our fitting procedure. Sections VI and VII contain the final results, their discussion, and the conclusions.

II. THE MODEL

A. The basic assumptions

We investigate the translational and rotational motion of a sphere that settles due to gravity onto a fixed (motionless) sphere of approximately the same radius a (cf. Fig. 1). Both spheres are surrounded by an incompressible viscous fluid. The Reynolds number of the fluid motion is low compared with unity. The fluid velocity $\boldsymbol{v}$ and pressure p satisfy the Stokes equations,

$$\eta \nabla^2 \boldsymbol{v} - \boldsymbol{\nabla} p = \boldsymbol{0}, \quad \boldsymbol{\nabla} \cdot \boldsymbol{v} = 0, \tag{1}$$

where η is the fluid viscosity. We assume that the stick boundary conditions hold, i.e., the fluid at the contact with a sphere surface moves with the same velocity as the sphere. The "external" forces and torques acting on the mobile particle, $\mathbf{F}_1$ and $\mathbf{T}_1$, are balanced by the "internal" hydrodynamic forces caused by the fluid. Since the Stokes equations (1) are linear, the particle translational and angular velocities, $\mathbf{U}_1$ and $\boldsymbol{\Omega}_1$, depend linearly on $\mathbf{F}_1$ and $\mathbf{T}_1$,

$$\begin{pmatrix} \mathbf{U}_1 \\ \boldsymbol{\Omega}_1 \end{pmatrix} = \boldsymbol{\zeta}_{11}^{-1} \cdot \begin{pmatrix} \mathbf{F}_1 \\ \mathbf{T}_1 \end{pmatrix}. \tag{2}$$

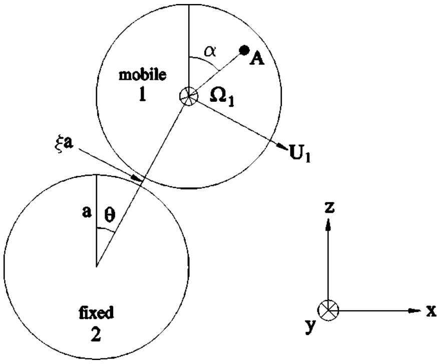

FIG. 1. The system and notation. Sphere 2 is fixed and sphere 1 moves with the angular and translational velocities, $\boldsymbol{\Omega}_1 = (0,\Omega_{1y},0)$ and $\mathbf{U}_1 = (U_{1x},0,U_{1z})$. The position of the moving sphere center, with respect to the fixed sphere center, is parameterized by θ and ξ as $(2+\xi)\mathrm{a}(\sin\theta,0,\cos\theta)$.

For ideally smooth spheres, the components of the inverse of the two-particle hydrodynamic friction matrix $\boldsymbol{\zeta}_{11}$ [39], have been constructed from the solution to the Stokes equations and evaluated numerically as functions of the distance between the particles [1,8,10].

However, the surfaces of the real particles are rough with randomly distributed asperities of a different size and shape. It is not possible to evaluate exactly the friction matrix for such a complex geometry. As it has been mentioned in Introduction, the hydrodynamic repellent forces between the approaching spheres increase to infinity when the gap size tends to zero. Therefore, a question arises that how do typical minimal separations between the ideal, smooth spheres compare to the roughness of real particles—is it really necessary to go beyond the model of ideal, separated spheres. The affirmative answer to this question follows from the calculation of the motion of a smooth sphere in vicinity of the other smooth, fixed sphere. If initially the moving sphere is almost above the fixed one (as in our experiments), then the calculated hydrodynamic interactions between the smooth spheres would eventually lead at $\theta = \pi/2$ to unrealistically small separations between the surfaces, even smaller than the atom size, which certainly cannot be accepted [40]. Therefore we assume that in our experiments, the particles come so close to each other that the asperities on their surfaces come into mechanical contact. (For rough particles, unlike for the ideal spheres, there is no evidence that the lubrication forces would be sufficiently strong to prevent particles from touching.) To describe the system, we follow Davis [13] and approximate the real particles at contact by effective, ideally smooth spheres, separated by a thin liquid layer of an "averaged" constant thickness, under external mechanical contact forces in addition to gravity. This is an *ad hoc* assumption with no explanation in terms of any systematic effective theory. In the model, the settling motion of sphere 1 is driven by the following external forces $\mathbf{F}_1$ and torques $\mathbf{T}_1$ (see Fig. 1 for notation) [13,15].

(1) If there is no contact, then $\mathbf{T}_1 = 0$ and $\mathbf{F}_1$ is due to the gravity only, $\mathbf{F}_1 = (0,0,-G)$, where G is the weight minus the buoyancy. These formulas apply when sphere 1 approaches sphere 2 (i.e., for θ less than a "touching angle" θ_i) or when it moves apart (i.e., for $\theta > \pi/2$).

(2) If contact occurs, then the mechanical interaction of the touching surfaces supplements the gravity, $\mathbf{F}_1 = (P\sin\theta - R\cos\theta, 0, P\cos\theta + R\sin\theta - G)$ and $\mathbf{T}_1 = (0, R\mathrm{a}, 0)$, where the friction R is tangential and the reaction P is normal to the surface. These formulas apply for $\theta_i \leqslant \theta \leqslant \pi/2$.

We specify R and P by making three assumptions. First, at contact we introduce an effective, averaged distance between the surfaces, aξ, which does not change with θ: $\xi = \text{constant}$ (i.e., the component of the translational velocity along the line of the centers vanishes). Secondly, for θ between θ_i and a critical angle θ_s, which is related to the static friction, a pure rolling motion (i.e., without slip) takes place: $a\Omega_1 = U_1$, where $\Omega_1 \equiv |\mathbf{\Omega}_1|$ and $U_1 \equiv |\mathbf{U}_1|$. Finally, if $\theta_s \leqslant \theta \leqslant \pi/2$, then rolling with slip occurs, and the Coulomb's law gives $R = \mu_k P$, where μ_k is the kinetic friction coefficient [32–34].

B. Transition from pure rolling to rolling with slip

The assumptions presented in the preceding section and Eq. (2) allow to calculate the expressions for the reaction force P (that is, also of the load) and for the mechanical friction R,

$$P = G\cos\theta, \tag{3}$$

$$R = \begin{cases} \dfrac{\mu_s}{\tan\theta_s} G \sin\theta & \text{for pure rolling} \\ \mu_k G\cos\theta & \text{for rolling with slip.} \end{cases} \tag{4}$$

From Eq. (2) it follows that the static friction coefficient μ_s is related to the transition angle θ_s and to the normalized distance between the particle surfaces, ξ, by the following relation:

$$\tan\theta_s = \mu_s s, \tag{5}$$

where s depends logarithmically on ξ. In Appendix A the function s is specified in terms of components of the friction matrix $\boldsymbol{\zeta}_{11}$ [10] and its dependence on $\log_{10}\xi$ is depicted.

The nature of the contact depends on R/P, the ratio of the forces specified in Eqs. (3) and (4). This parameter changes with θ, as schematically shown in Fig. 2. During the pure rolling motion, the ratio R/P increases linearly with $\tan\theta$, until it reaches a critical value θ_s, which is related to the static friction coefficient μ_s by Eq. (5). At θ_s the rolling with slip starts, with a sudden decrease of R/P to μ_k, the value of the kinetic friction coefficient. For larger angles, $R/P = \mu_k$. Note that μ_k is not larger than μ_s [32,33].

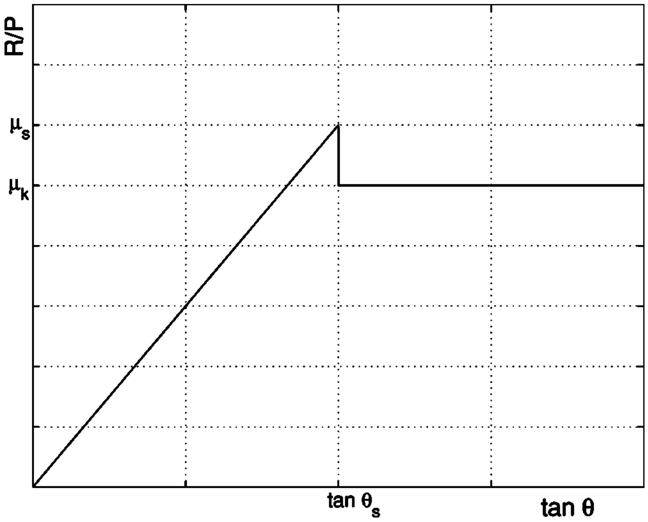

FIG. 2. The transition between pure rolling and rolling with slip corresponds to a discontinuous decrease of the friction-to-load ratio, R/P, from μ_s (the static friction coefficient) to μ_k (the kinetic friction coefficient).

C. Units

Distances are expressed in particle radii, a, and translational velocities are normalized by the Stokes velocity,

$$v_{st} = \frac{2}{9\eta} a^2 (\rho_p - \rho_f) g, \tag{6}$$

where ρ_p and ρ_f are the densities of the moving particle and of the fluid, respectively, and g is the gravitational acceleration.

Time τ is measured in the Stokes units, τ_{st}, defined as the time for an isolated sphere in unbounded fluid to move along a distance equal to its radius,

$$\tau_{st} = \frac{a}{v_{st}}. \tag{7}$$

Angular velocities are therefore normalized by $1/\tau_{st} = v_{st}/a$.

D. The translational and the angular velocities at the contact

In Ref. [15] the translation of sphere 1 was evaluated from Eq. (2). Since there is no motion along the line of the sphere centers, U_{1x} and U_{1z} are expressed in terms of the transverse velocity U_1 as

$$U_{1x} = U_1 \cos\theta, \quad U_{1z} = -U_1 \sin\theta. \tag{8}$$

Now we calculate the rotation, also from Eq. (2). The total motion due to gravitational, hydrodynamic, and contact forces is given by Eq. (8) and the following formulas.

(1) For pure rolling at contact ($\theta_i < \theta < \theta_s$),

$$\frac{\Omega_1}{U_1} = 1, \tag{9}$$

$$U_1 = v_0 r \sin\theta. \tag{10}$$

(2) For rolling with slip at contact ($\theta_s < \theta < \pi/2$),

$$\frac{\Omega_1}{U_1} = (1-d)\frac{\sin\theta + e\mu_k\cos\theta}{\sin\theta - d\mu_k\cos\theta} \leqslant 1, \tag{11}$$

$$U_1 = v_0 t(\sin\theta - \mu_k d\cos\theta). \tag{12}$$

Here d,e,r,t are positive coefficients determined by the two-sphere friction matrix $\boldsymbol{\zeta}_{11}$. They depend logarithmically on ξ (cf. Appendix A for the details).

In Eqs. (10) and (12), $v_0 < 1$ is a parameter that accounts for the effect of the container walls [15], which slow down the motion. Since contact takes place in the middle part of the container, we assume that $v_0 \approx \text{const}$.

In Fig. 3 we plot U_1 and Ω_1 due to rolling with slip versus θ for different values of ξ, μ_k, and v_0. Figure 3 illustrates why the comparison between the experimental and the theoretical *translational* velocities only is not sufficient to determine the set of the model parameters accurately and explains why it is helpful to measure also the *angular* veloci-

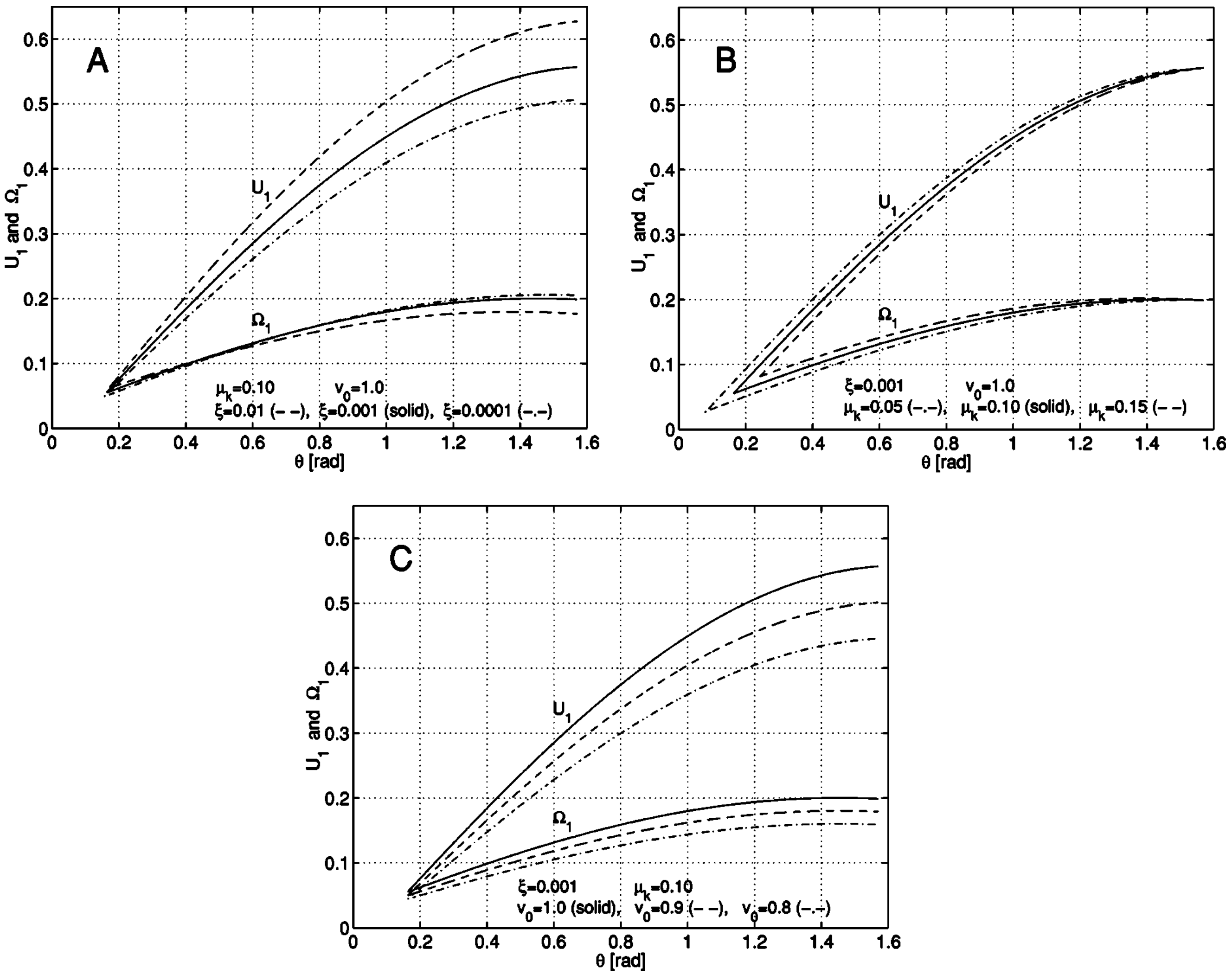

FIG. 3. Translational and angular velocities for rolling with slip, normalized by v_{st} and v_{st}/a, respectively. Sensitivity to a change of the model parameters ξ, μ_k, and v_0 is shown. The full model of the contact is obtained if the part where $\theta<\theta_s$ is replaced by the pure rolling with $\Omega_1=U_1\sim\sin\theta$; in general, with a jump at $\theta=\theta_s$, where the slip stops.

ties. That is, Figs. 3(a) and 3(c) indicate that one could match the same experimental U_1 points by different sets of the model parameters. Indeed, if ξ and v_0 generated a good fit, then also ξ' and v_0' would generate a reasonable fit, if the increase of ξ (i.e., $\xi'>\xi$) is compensated by the suitable decrease of v_0 (i.e., $v_0'<v_0$), and vice versa. But this remark holds for the U_1 points only. Both sets (ξ,v_0) and (ξ',v_0') would not match the same experimental set of Ω_1 points. This example illustrates that the measurement of the rotational motion in addition to the translational one allows to decrease the uncertainty of the model parameters following from the fitting procedure.

It is convenient to represent rotation in terms of Ω_1/U_1, because in this way we eliminate v_0, so that only three parameters of the rotation model are left in Eqs. (10) and (11): ξ, μ_k, and θ_s. In Fig. 4 we plot Ω_1/U_1 due to rolling with slip, given by Eq. (11), versus θ, for different values of ξ and μ_k. If θ is close to $\pi/2$, then $\Omega_1/U_1\approx 1-d$ is independent of μ_k and sensitive to a logarithmic change of ξ. Conversely, the smaller the θ, the stronger the dependence of Ω_1/U_1 on μ_k.

If $\mu_s>\mu_k$, then U_1, Ω_1, and Ω_1/U_1 are discontinuous functions of θ at θ_s, i.e., at the transition from pure rolling to rolling with slip. We calculate values and signs of the relative jumps [i.e., the difference of the corresponding values at θ_s, given by Eqs. (11) and (12) and by Eqs. (9) and (10), divided by the values given by Eqs. (9) and (10)]. The relative jumps are the following.

(1) For the translational velocity U_1,

$$(1-\mu_k/\mu_s)(t/r-1)>0.$$

(2) For the angular velocity Ω_1,

$$\Omega_1,\ (\mu_k/\mu_s-1)\,(1-d)\,t\,e\,(rs)^{-1}<0.$$

(3) For the ratio Ω_1/U_1,

$$(\mu_k/\mu_s-1)\,s\,[(1-\mu_k/\mu_s)+r/(t-r)]^{-1}<0.$$

By comparison, for a sphere rolling with slip along an inclined plane in the Stokes flow [41], dependence of the rotational and translational velocities as well as of their ratio on the inclination angle θ (and also on μ_k, ξ) is analogous

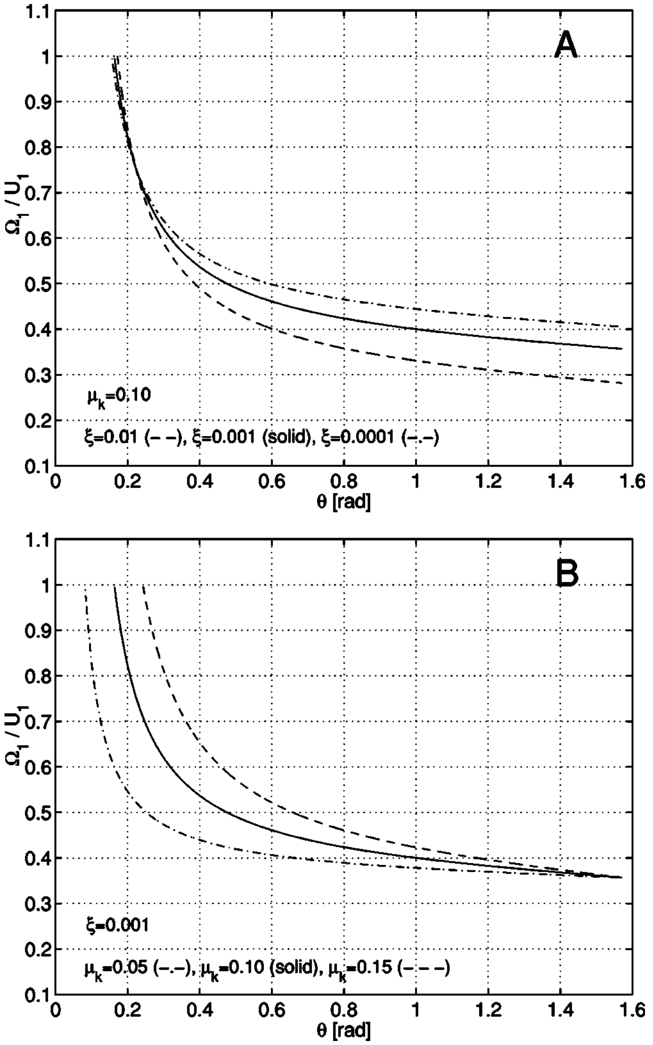

FIG. 4. Theoretical predictions for the rolling with slip. The full model of the contact is obtained if the part where $\theta<\theta_s$ is replaced by the pure rolling with $\Omega_1/U_1=1$; in general, with a jump at $\theta=\theta_s$, where the slip stops.

to the one presented in Figs. 3 and 4, as illustrated and discussed in Appendix B. The pure rolling motion and the jumps are also similar.

E. The lubrication phenomena

In our model, the interactions between the real particles with rough surfaces are described as effective hydrodynamic plus contact interactions between smooth spheres. The concept of an effective smooth surface, which accounts for the hydrodynamic interactions of the real rough one, has been extensively investigated in other contexts, i.e., for a rough sphere falling away from a smooth plane [42] and for a rough plane in shear flow [43–45].

At the contact, the distance between the effective, smooth sphere surfaces, ξ, is very small, and the dominant contribution to the friction matrix $\boldsymbol{\zeta}_{11}$ and its inverse, which appears in Eq. (2), comes from the lubrication asymptotic expansion in small values of ξ [46,47]. The components of $\boldsymbol{\zeta}_{11}$ responsible for the transverse motion behave as $A\ln\xi+B+C\xi\ln\xi$, where A, B, C are constants, given, e.g., in Refs. [1,10], and listed in Appendix A. As a result, the expressions d,e,r,s,t in Eqs. (5) and (10)–(12) are sensitive to changes of $\log_{10}\xi$ (or $\ln\xi$) rather than to changes of ξ. In addition, functions $d(\log_{10}\xi)$, $r(\log_{10}\xi)$, $s(\log_{10}\xi)$, $t(\log_{10}\xi)$, which determine the translational motion, are flat. This property is illustrated in Fig. 11 in Appendix A. For ξ varying between 3×10^{-5} and 10^{-2} (more than by a factor of 300), the functions d,r,s,t change only by a factor of 1.1–1.3.

As it has been pointed out in Ref. [15], Eqs. (5), (10), and (12) are not sufficient to determine what is the value of ξ from measurements of the translational motion of sphere 1. The wide range of admissible ξ given in Ref. [15] was estimated in a different way—by the requirements that ξ is smaller than the height of the surface asperities, ξ_{max}, and that ξ cannot be lower than ξ_{min} determined from the condition that $v_0<1$, i.e., the walls effectively decrease the Stokes velocity.

The main idea of this paper is to analyze the rotational motion of sphere 1, together with the translational one, in order to provide a more accurate way to compare the model to the experiment. Such a refinement is expected, because the experiment provides more information and in addition, as illustrated in Fig. 11 in Appendix A, the function e, which determines the angular velocity at the rolling with slip in Eq. (11), is more sensitive to changes of $\log_{10}\xi$ than d,r,s,t, which specify the translational motion.

III. THE EXPERIMENT

This section is devoted to present the experimental setup, which combines a new video image processing system for measurement of rotational and translational motions with an interferometric technique (developed in Refs. [35,37]) for accurate detection of the translational motion. Both methods are applied simultaneously.

The moving sphere is a steel ball bearing with diameter $d=6.35$ mm, departure from sphericity $\lesssim0.5$ μm and density 7800 $\mathrm{kg\,m^{-3}}$. Its surface is smooth, viz., the height of its asperities typically does not exceed 1 μm, and arithmetic roughness $Ra=0.013$ μm. The fixed sphere is a polyacetal ball bearing with diameter $\mathrm{d}=6.30\pm0.02$ mm and the height of its surface asperities is around 10 μm. Both particles are immersed in a silicon oil (Rhodorsyl 47V100000 by Rhône-Poulenc), with a kinematic viscosity $\nu=0.1$ $\mathrm{m^2/s}$ and density 974 $\mathrm{kg\,m^{-3}}$ at 25 °C. The fluid flow is slower than $v\approx1.5$ $\mathrm{mm\,s^{-1}}$, so that the Reynolds number is less than $vd/\nu\lesssim10^{-4}$. The cell is a closed cuboid with a square horizontal cross section of 50 mm×50 mm and a height of 40 mm. The motionless sphere is fixed in the center of the cell with a horizontal nonmagnetic metallic rod.

The initial position of the steel sphere is controlled with a magnet located on the upper side of the top wall, so that the initial distance of the sphere from the vertical line specified by the fixed sphere center is typically around 100 μm (1) to obtain later very small separations between the particle surfaces and to allow them to get into contact and (2) to control the motion such that it occurs in the vertical plane perpendicular to the viewing axis of the video camera, with a typical deviation angle not exceeding 5°.

Therefore, it is sufficient to trace the rotational motion of the steel sphere through subsequent positions of a dot painted on its surface. Another dot is painted on the fixed sphere to determine the positions of both sphere centers more accurately. The dots are kept away from the contact area.

The video camera is a DCR-TRV9E model by Sony. The number of pixels per frame is 720×576 and the chosen enlargement ratio is such that the vertical frame size corresponds to four particle diameters. A standard rate of 25 frames/s is sufficient to record the motion, since during 1/25 s the sphere is moving at most 1/150 of its diameter, that, is at most one pixel per frame. The time is recorded automatically in each frame.

The positions of both sphere centers and of the dots in each frame are extracted from video images using a software developed specifically for this experiment. The three colors (red, green, and blue) recorded by the camera are treated separately. Color intensity levels of each pixel are in the range [0, 255]. The classical gradient method is used to determine the edges of the spheres. The centers of the yellow dots are determined as barycenters of the pixels for which the color intensity is above a given threshold. The uncertainty of the measured positions of the sphere center and the dot center is around one pixel.

As a result, we obtain the positions of the dots and of both spheres centers as functions of time. We use these data to calculate also the time dependence of the relative positions and of the angles θ and α denoted in Fig. 1. Examples of such an experimental relation will be given in Sec. V C in Fig. 6.

Simultaneously with the video detection, we also measure the translational motion of the sphere in the same way as in Ref. [15]. That is, we use the laser interferometric technique from Ref. [35] to record the vertical translational velocity in the standard way. The typical sensitivity of the measured vertical displacement is of the order of 100 nm. The vertical laser beam is reflected back by the moving steel particle as a cone of light, which changes its orientation and shape when the sphere moves horizontally with respect to the laser beam. These changes are detected by a system of photodiodes, and the corresponding horizontal displacements are evaluated [35].

Interferometric measurements require that the moving sphere surface should efficiently reflect the laser beam. However, a consequence is that there are also parasitic reflections of the surrounding light, so that the image analysis becomes difficult to perform. Nevertheless, the benefits from the simultaneous interferometric detection are significant since the gained information allows to improve the accuracy of video measurement in the three following ways.

(1) First, the interferometric technique is used to trace the plane of the motion (denoted as xz in Fig. 1) and to check how much it differs from the camera plane of view. Since we control if the sphere was released in the right plane with an accuracy of 20 μm [35], we are able to make the angle between both planes reasonably small. We perform several experiments and retain only those for which this angle does not exceed 5°.

(2) Second, the interferometric measurements are used to calibrate the video image; in particular, to transform the vertical and horizontal dimensions of a pixel into mm.

(3) Third, the interferometric measurement is used to estimate the Stokes velocity. Since the fluid viscosity is very sensitive to the temperature changes, which are not measured in our experiments, we use the method described in Refs. [36,48] rather than the standard formula (6). That is, the Stokes velocity is measured by comparing accurate experimental results for the motion of a sphere towards (or away from) a plane wall with the exact analytical result by Brenner [49] and Maude [50]. The precision on this experimental Stokes velocity is estimated to be around 1%.

IV. HOW TO CHOOSE ONE OF THE VARIOUS THEORETICAL REPRESENTATIONS OF THE MOTION?

A. The difficulties of a fitting procedure

In the previous studies of the hydrodynamic and contact interactions between two spheres, or a sphere and a plane, the fitting of the motion predicted by the model to that measured in the experiment was based on a comparison of the theoretical and the experimental velocities [13,15,41]. However, the procedure of extracting $\Omega_1 = d\alpha/d\tau$ and $U_1 = 2\,d\theta/d\tau$ from time derivatives of video experimental data for θ and α has its own error bars that decrease precision. A better method would be to exploit the relation

$$2\frac{\Omega_1}{U_1} = \frac{d\alpha}{d\theta}, \tag{13}$$

and compare the experimental and theoretical plots of α versus θ for each trial. Integration of Eqs. (9) and (11) and the continuity of $\alpha(\theta)$ give the following.

(1) For pure rolling,

$$\alpha(\theta) = 2(\theta - \theta_i) + \alpha_i, \tag{14}$$

(2) For rolling with slip,

$$\alpha(\theta) = E \ln\frac{\sin\theta - d\,\mu_k\cos\theta}{\sin\theta_s - d\,\mu_k\cos\theta_s} + F(\theta - \theta_s) + 2(\theta_s - \theta_i) + \alpha_i, \tag{15}$$

where θ_i is the angular position of the moving sphere center at the beginning of the contact, $\alpha_i = \alpha(\theta_i)$, and the constants E and F depend on ξ and μ_k,

$$E = 2\,(1-d)\mu_k \frac{d+e}{d^2\,\mu_k^2 + 1}, \tag{16}$$

$$F = 2\,(1-d)\frac{1 - de\mu_k^2}{d^2\,\mu_k^2 + 1}. \tag{17}$$

The functions $d(\log_{10}\xi)$ and $e(\log_{10}\xi)$ are given in Appendix A.

The dependence of α on θ while rolling with slip is shown in Fig. 5. Globally, the rotation velocity is larger for the smaller separation between spheres and for the larger friction coefficient. Locally, for small angles the slope (which is proportional to the ratio of the angular and the

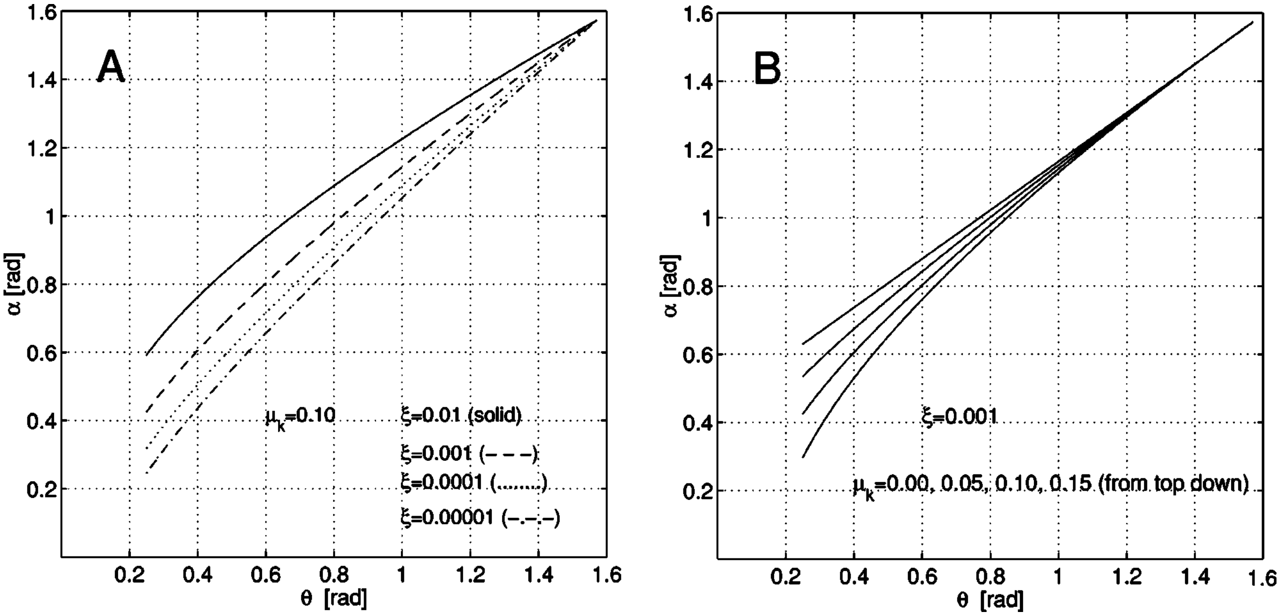

FIG. 5. Theoretical predictions for the angular positions of the dot on the moving sphere rolling with slip along the fixed sphere (cf. Fig. 1 for the notation). A: Sensitivity to a change of ξ. B: Sensitivity to a change of μ_k.

translational velocities) depends on μ_k, but it is practically independent of ξ. On the contrary, for angles close to $\pi/2$ the slope depends on ξ, but it is practically independent of μ_k.

Note that the curves in Fig. 5 can be shifted and cut (or extended) to match the values of θ_s and α_s, which correspond to the beginning of the rolling-with-slip motion. The pure rolling could be also included in Fig. 5, if for $\theta<\theta_s$ the straight line of the slope 2 was drawn through the point (θ_s,α_s). The intersection of this line with the vertical line $\theta=\theta_i$ specifies the initial angular position of the dot, α_i.

Minimization of the squared distances between the model curve and the experimental points on the plot α versus θ would allow to analyze the rotational motion. However, to reach the highest accuracy, we want to fit *at the same time* also the measurements of the translational motion. To this goal we use another theoretical representation of the motion, also based on the comparison of experimental and theoretical positions rather than of their derivatives (i.e., velocities).

B. The quantities to be fitted

In this paper we evaluate from the model the expressions for those time-dependent variables, which we have measured, and then we *simultaneously* minimize the distances between all the corresponding theoretical and experimental functions. The set of independent quantities, which are detected by our video measurements, is the following (see Fig. 1).

(1) $\tilde{\tau}_k$, $k=1,\dots,L$—times of subsequent measurements.

(2) $(\tilde{X}_k,\tilde{Z}_k)$—coordinates of the moving sphere center, measured with respect to the fixed sphere center at time $\tilde{\tau}_k$.

(3) $(\tilde{x}_k,\tilde{z}_k)$—coordinates of the dot on the moving sphere, measured with respect to the moving sphere center at time $\tilde{\tau}_k$.

Unlike all the previous theoretical expressions, the above quantities are still *dimensional*, since before normalizing them, we first need to specify the particle radius and the Stokes velocity from the measurements.

C. Positions versus time

In this section we specify theoretical expressions for the corresponding relative *dimensionless* positions of the moving sphere center (X,Z) and of the dot (x,z),

$$(X,Z)=(2+\xi)\,(\sin\theta,\cos\theta), \tag{18}$$

$$(x,z)=R_d(\sin\alpha,\cos\alpha). \tag{19}$$

The angles α and θ are specified in Fig. 1, and R_d characterizes the distance between the dot and the moving sphere center on the video frame. Since the motion takes place in the plane of the video frame, $R_d=\text{const}$.

The dependence of θ on the dimensionless time τ is obtained by integration of Eqs. (10) and (12).

(1) For pure rolling [for $\tau<\tau_s$, i.e., for $\theta<\theta_s=\theta(\tau_s)$]

$$\tan\frac{\theta}{2}=T\exp[D(\tau-\tau_i)], \tag{20}$$

where

$$T=\tan\frac{\theta_i}{2},\qquad D=v_0\frac{r}{(2+\xi)}, \tag{21}$$

with $\theta_i=\theta(\tau_i)$, and the time τ_i corresponds to the beginning of the contact.

(2) The transition angle θ_s is specified by Eq. (20),

$$\tan\frac{\theta_s}{2}=T\exp[D(\tau_s-\tau_i)]. \tag{22}$$

(3) For rolling with slip (for $\tau > \tau_s$, i.e., for $\theta > \theta_s$)

$$\tan\frac{\theta}{2} = \frac{Y(\tau)+C}{1-CY(\tau)}, \tag{23}$$

where

$$Y(\tau) = \frac{\tan\frac{\theta_s}{2} - C}{1 + C\tan\frac{\theta_s}{2}} \exp[A(\tau-\tau_s)], \tag{24}$$

$$A = v_0 t \frac{1+B^2}{2(2+\xi)B}, \quad C = \frac{1-B}{1+B}, \tag{25}$$

$$B = [(\mu_k d)^2 + 1]^{1/2} - \mu_k d. \tag{26}$$

The function $\alpha(\tau)$ is obtained when Eqs. (20)–(26) (which specify the time dependence of θ) are combined with Eqs. (14) and (15) (which determine α in terms of θ).

V. COMPARISON OF THE MODEL AND THE EXPERIMENT

A. Rescaled sphere radius

In Sec. II C we have used the effective ‘‘theoretical’’ radius of the smooth sphere, a, to normalize positions. Now we determine the ‘‘experimental’’ radius from the relation

$$a = \frac{1}{2N} \sum_{k=i}^{N+i-1} (\tilde{X}_k^2 + \tilde{Z}_k^2)^{1/2}, \tag{27}$$

where the indices $k=i$ and $k=o=i+N-1$ correspond to the beginning and to the end of the contact, respectively.

The dimensionless experimental positions used in the fitting procedure are always measured in terms of a. In principle, the experimental radius, which we measure, is slightly larger than the theoretical one, that is, $a=(1+\xi/2)$a. In practice, $\xi \lesssim 1\%$; in the model, we neglect the comparable difference between the sizes of both spheres used in the experiment, therefore we also approximate $a \approx$ a.

B. The fitting procedure

The model parameters to be determined from the experiment are ξ, the effective distance between the sphere surfaces, μ_k, the kinetic friction coefficient, v_0, the effective Stokes velocity, and τ_s, the time of the transition from pure rolling to rolling with slip. To make use of Eqs. (18)–(26), we need to specify from the experiment also the time interval (τ_i, τ_o), which corresponds to the contact, the distance R_d, and the initial position of the dot given by α_i and θ_i.

To determine τ_i and τ_o, we use the interferometric measurements, which have been performed simultaneously with the video recording. In particular, τ_i corresponds to the minimum of the vertical translational velocity.

We specify R_d in a similar way as a in Eq. (27); however, now we use a to make R_d dimensionless,

$$R_d = \frac{1}{a\,N} \sum_{k=i}^{N+i-1} (\tilde{x}_k^2 + \tilde{z}_k^2)^{1/2}, \tag{28}$$

where $\tilde{x}_k$, $\tilde{z}_k$ are the experimental relative positions of the dot (with respect to the moving sphere center) during the motion at contact.

The angles α_i and θ_i can be directly measured in the experiment, but with large error bars. To increase the accuracy of the fit, we allow for small changes of the parameters α_i and θ_i, so as we include them also as the minimization parameters, together with ξ, μ_k, v_0, and τ_s.

In our fitting procedure, we aim towards the least averaged squared error per point, so we minimize the following function:

$$F = \sum_{k=i}^{N+i-1} \frac{\Delta_k^2}{4(N_r+N_{rs})}, \tag{29}$$

$$\Delta_k^2 = (X_k - \tilde{X}_k/a)^2 + (Z_k - \tilde{Z}_k/a)^2 + (x_k - \tilde{x}_k/a)^2 + (z_k - \tilde{z}_k/a)^2, \tag{30}$$

where $\tilde{X}_k$, $\tilde{Z}_k$, $\tilde{x}_k$, $\tilde{z}_k$, the experimental positions at times τ_k, are compared with the corresponding theoretical values, $X_k = X(\tau_k)$, $Z_k = Z(\tau_k)$, $x_k = x(\tau_k)$, $z_k = z(\tau_k)$.

In the minimization procedure the number of the experimental points at the contact, $N = N_r + N_{rs}$, is fixed, and specified by the choice of τ_i and τ_o. However, N_r and N_{rs} are the numbers of the experimental points, which are assigned *by the fitting* to the pure rolling and rolling with slip, respectively. That is, N_r and N_{rs} depend on the value of τ_s, which is the outcome of the minimization.

In the fitting the difference between the static and kinetic friction coefficients is automatically non-negative, $\mu_s \geqslant \mu_k$. The minimization is performed by our MATLAB numerical program.

C. The results

This section consists of three parts. First, we perform the detailed analysis of an exemplary experimental trial 17 (the one with the smallest minimal value of F). Then we present values of the model parameters obtained by the same method for another trials. Finally, we estimate the error bars of the model parameters for the trial 17.

For trial 17 the basic units are

$$a = 3.16 \pm 0.01 \text{ mm}, \tag{31}$$

$$v_{st} = 1.49 \pm 0.02 \text{ mm/s}, \tag{32}$$

$$\tau_{st} = \frac{a}{v_{st}} = 2.12 \pm 0.03 \text{ s}. \tag{33}$$

The above values are used to normalize all the dimensional quantities for this trial. In particular,

$$R_d = 0.817 \pm 0.007, \tag{34}$$

$$\tau_o - \tau_i = 18.77 \pm 0.02. \tag{35}$$

The error bars of about 0.3% and 0.9% for a and R_d, respectively, are estimated as the standard deviations of the expressions (27) and (28). The method used to determine the Stokes velocity v_{st} is explained in Sec. III.

The error bars of τ_i and τ_o in Eqs. (35) correspond to the time separation between video frames. For convenience, we shifted the time coordinates to get $\tau_i = 0$.

The question is how to find the minimum of function F, given by Eq. (29). The first approach is to use the standard MATLAB minimization procedure, in which the downhill simplex method due to Nelder and Mead [51] is applied. We get $F_{min} \approx 5 \times 10^{-5}$. However, the corresponding model parameters are not specified uniquely. The difficulty is that close to its minimum, function F is flat (for example, in a wide range of $\log_{10}\xi$, and the suitably adjusted range of v_0, cf. Sec. II D). To evaluate F_{min} by the standard MATLAB procedure, one needs to specify "input" values of the model parameters. Different input choices result in a certain dispersion of F_{min}, which is of the order of a few percent, and the corresponding dispersion of the model parameters.

To describe this ambiguity more rigorously, we calculate values of function F on over two million grid points in the four-dimensional space of the model parameters. We take τ_s, $(\mu_s - \mu_k)$, $\log_{10}\xi$, and v_0 as the coordinates and a uniform distribution of the grid points along each axis.

To specify the grid units, we first estimate ΔF, the accuracy of F, as $\Delta F/F \approx 1/\sqrt{N} \approx 3\%$, where $N \approx 1000$ is the number of the measurement points at the contact. Next we use $\Delta F/F$ to construct the spacing along each axis of the grid. That is, we start from a preliminary grid, and we optimize it in the following way. We find the coordinates, which correspond to the smallest value of F on the preliminary grid, i.e., F_{min}^{grid}. We estimate that at the real minimum, $F = F_{min} \geqslant F_{min}^{grid} - \Delta F_{min}^{grid}/2$, where ΔF_{min}^{grid} is the largest difference between F_{min}^{grid} and the value of F at the eight closest points of the grid. We compare $\Delta F_{min}^{grid}/F_{min}^{grid}$ with $2\Delta F/F$, i.e., with $\approx 6\%$, and optimize the preliminary grid until $\Delta F_{min}^{grid}/F_{min}^{grid} \lesssim 6\%$.

To specify the range of the model parameters, which may correspond to the minimum of F, we search for all the grid points, for which $F \leqslant F_{min}^{grid} + \Delta F_{min}^{grid}/2$, i.e., for which $(F - F_{min}^{grid})/\Delta F_{min}^{grid} \leqslant 3\%$. For each coordinate, we calculate its minimal and maximal values over all the selected grid points [51]. We get the following range of the model parameters:

$$\mu_k = 0.11 - 0.12, \tag{36}$$

$$\xi = (2.4 - 4.1) \times 10^{-3}, \quad -\log_{10}\xi = 2.4 - 2.6, \tag{37}$$

$$\tau_s = 7.4 - 8.6, \tag{38}$$

$$v_0 = 0.83 - 0.84. \tag{39}$$

The minimization refines the accuracy of the measured values of θ_i and α_i as

$$\theta_i \approx 0.06, \quad \alpha_i \approx 0.23. \tag{40}$$

From Eqs. (5), (22), and (39) we get

$$\theta_s = 0.19 - 0.22, \quad \mu_s = 0.11 - 0.13. \tag{41}$$

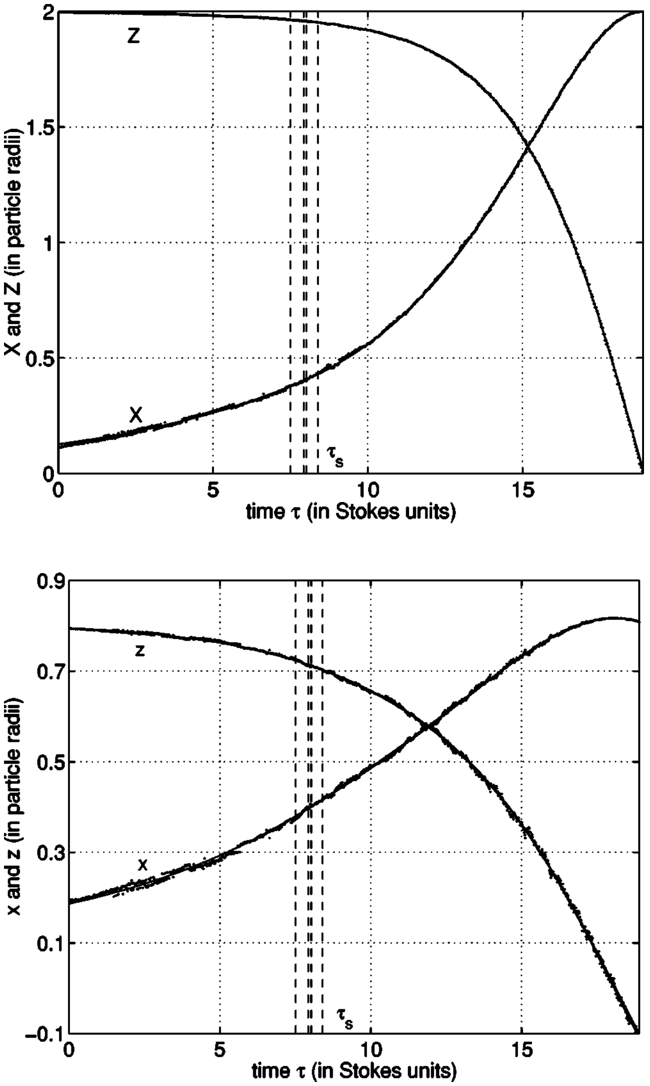

FIG. 6. Top: Translational motion. Relative positions of the moving sphere center with respect to the fixed sphere center versus time. Bottom: Rotational motion. Relative positions of the dot on the moving sphere with respect to the moving sphere center versus time. Dots: the experimental data; solid lines (superimposed): theoretical relation with $(\mu_k, \xi, v_0, \tau_s) \approx (0.11, 0.0030, 0.83, 7.5)$, (0.11, 0.0032, 0.83, 8.4), (0.11, 0.0025, 0.84, 7.9), and (0.12, 0.0038, 0.83, 8.0); 1 pixel≈0.015. The transition from pure rolling to rolling with slip is marked by vertical dashed lines.

In Fig. 6 the experimental data $(\tilde{X}_k, \tilde{Z}_k)/a$, $(\tilde{x}_k, \tilde{z}_k)/a$, and the fitted theoretical values $[X(\tau_k), Z(\tau_k)]$, $[x(\tau_k), z(\tau_k)]$ are plotted.

The fitting procedure described above has been applied to determine the model parameters for eight experimental trials performed in the same system. The results are given in Table I.

To discuss the error bars of the obtained model parameters, we concentrate on the analysis of the exemplary trial 17 with the corresponding values given in Eqs. (31)–(41). Comparison of F_{min} with σ^2, the squared standard deviation of a single measurement point (e.g., of X), provides an assessment of the goodness of fit [51]. $F_{min} \approx \sigma^2$ corresponds

TABLE I. The model parameters μ_k, μ_s, v_0, $\log_{10}\xi$ obtained for eight experimental trials performed in the same system. The fitting procedure described in Sec. V C has been used. The corresponding values of ξ, τ_s, and θ_s are also given for comparison (however, note that only four model parameters are independent). Value of $\sqrt{F_{min}}\times 10^2$ is the averaged difference between the model and the experiment per point and $\sigma\times 10^2$ is the standard deviation of a single measurement point (both are expressed in particle radii: in these units 1 pixel $\times 10^2 \approx 1.5$).

Trial no.	4	6	7	10	11	12	14	17
μ_k	0.11–0.12	0.11–0.13	0.14–0.15	0.12–0.14	0.11–0.13	0.12–0.13	0.10–0.11	0.11–0.12
μ_s	0.11–0.14	0.11–0.14	0.14–0.17	0.13–0.17	0.11–0.15	0.12–0.16	0.10–0.13	0.11–0.13
$v_0\times 10^2$(in %)	79–82	81–83	80–83	80–84	77–79	77–79	83–85	83–84
$-\log_{10}\xi$	2.2–2.7	2.4–2.9	2.4–2.8	2.2–2.9	2.0–2.5	1.9–2.4	2.4–2.8	2.4–2.6
$\xi\times 10^3$	2.0–6.0	1.3–4.3	1.5–4.4	1.4–6.5	3.5–10.2	4.2–11.7	1.7–3.9	2.4–4.1
τ_s	8–10	8–10	10–11	9–11	9–10	8–10	7–8	7–9
θ_s	0.18–0.23	0.19–0.24	0.23–0.28	0.21–0.28	0.19–0.25	0.20–0.26	0.16–0.21	0.19–0.22
$\sqrt{F_{min}}\times 10^2$	1.5	1.4	1.2	2.1	1.8	1.6	1.2	0.7
$\sigma\times 10^2$	1.8	1.8	1.4	1.7	1.8	1.8	0.9	1.1

to $\sigma\approx 0.5$ pixel, in agreement with the slightly higher than average precision of this particular trial (see Table I).

The model parameters, calculated in Eqs. (36)–(41), are characterized by an uncertainty, which is now estimated by a Monte Carlo simulation of 12 000 "synthetic data sets" [51]. The random draws have the normal distribution with the average equal to the real measurements ($\tilde{X}_k$, $\tilde{Z}_k$, $\tilde{x}_k$, $\tilde{z}_k$), $k=1,\dots,N$, and with the standard deviation equal to σ. Simultaneously, we also simulate the experimental coefficients, which are needed as an additional input to the fitting procedure.

Next, for each "synthetic set of data and coefficients," we perform the same procedure for estimation of the model parameters [51], as was performed on the actual experimental data and coefficients by the MATLAB minimization in Sec. V B. Using standard confidence levels [51], we looked for the upper limit of F values, which would correspond to 68.3% of the points in the space of the model parameters. We found it to be equal to $3.31F_{min}$. The selected points with $F_{min}\leqslant F\leqslant 3.31F_{min}$ defined the confidence region in the space of the model parameters. The projection of this confidence region $F<3.31F_{min}$ onto μ_k axis, μ_s axis, $\log_{10}\xi$ axis and v_0 axis gives the following estimations for the uncertainty of model parameters for trial 17, with the 68.3% confidence level:

$$\begin{aligned}&\text{error bars for } \mu_k\text{: } (0.10,0.13),\\ &\text{error bars for } \mu_s\text{: } (0.11,0.16),\\ &\text{error bars for } (-\log_{10}\xi)\text{: } (2.02,2.86),\\ &\text{error bars for } v_0\text{: } (0.80,0.85).\end{aligned} \tag{42}$$

Therefore we also have

$$\begin{aligned}&\text{error bars for } \xi\text{: } (0.001,0.009),\\ &\text{error bars for } \theta_s\text{: } (0.18,0.26).\end{aligned} \tag{43}$$

The model parameters vary from trial to trial (see Table I) in a wider range than the uncertainty limits (42) for trial 17. However, the corresponding uncertainty limits for the other trials may be larger than those given by Eq. (42), because for trial 17 σ is smaller than for the averaged trial (see Table I). Note that reflections of light may introduce also some systematic errors of the automatic detection of the positions (smaller than one pixel for trial 17, and not exceeding two pixels for the other trials).

We expect that the experimental errors explain a paradox, which can be seen in Table I. That is, for trials 11 and 12 the fitting gives for the effective gap sizes $\xi=0.003$–0.010 and $\xi=0.004$–0.012, respectively. Therefore separations, which are three to four times larger than the estimated height of asperities on the fixed sphere (i.e., 0.003), are admissible together with the gap sizes comparable with the roughness.

VI. DISCUSSION OF THE RESULTS

Following the theoretical analysis displayed in Fig. 5, we plot in Fig. 7 the experimental and theoretical angular positions α versus θ. The theoretical curve is specified by Eqs. (14) and (15), with the parameters given in Eqs. (31)–(41) as the result of the fitting procedure.

To compare the experimental and theoretical velocities we calculate the numerical derivative of the experimental data for the angles θ and α versus time τ. Following a standard idea, the data are fitted in the sense of least squares with a polynomial of degree $L=3$, using $K=250$ additional points to the right and $K=250$ additional points to the left of each desired τ value. As in Ref. [51], the estimated derivative is the derivative of this polynomial, taken at τ [52].

The numerical derivatives of the experimental data, $U_1=2\,d\theta/d\tau$ and $\Omega_1=d\alpha/d\tau$, are plotted in Fig. 8, and their ratio Ω_1/U_1 in Fig. 9. (Compare also with the theoretical families of curves for rolling with slip in Figs. 3 and 4, respectively.)

In Fig. 8 the experimental velocities are interpreted by the model. For small angles θ the experimental translational and angular velocities coincide, in agreement with the pure rolling motion, for which $U_1=\Omega_1\sim\sin\theta$. For the angles θ larger than a transition value θ_s, the translation dominates the rotation, in agreement with the rolling-with-slip model, see Eqs. (11) and (12).

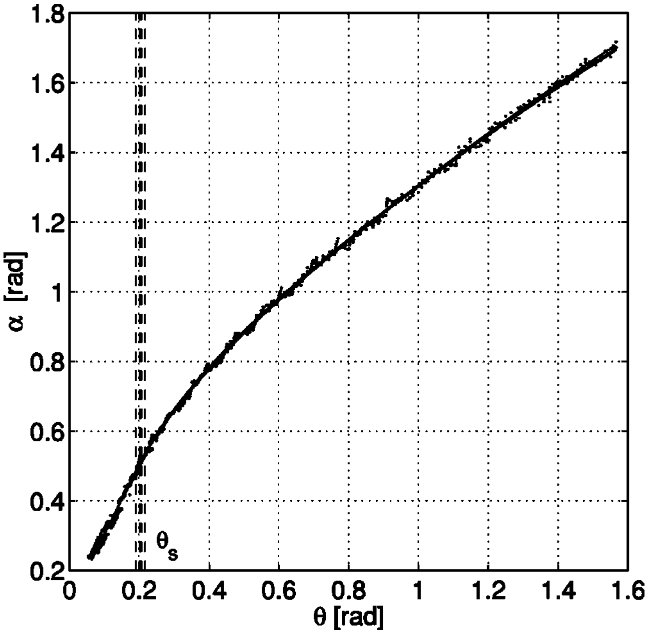

FIG. 7. The angular positions of the dot on the moving sphere versus the angular positions of the mobile sphere center (cf. Fig. 1 for the notation). Dots: the experimental data; solid lines (superimposed): theoretical relation with (μ_k,ξ,v_0,θ_s) $\approx(0.11,0.0030,0.83,0.19)$, (0.11, 0.0032, 0.83, 0.22), (0.11, 0.0025, 0.84, 0.20), and (0.12, 0.0038, 0.83, 0.21). The transition from pure rolling to rolling with slip is marked by vertical dashed lines.

The ratio of the experimental velocities, given by Eqs. (9) and (11), is displayed in Fig. 9. For small angles θ, a large discrepancy between the model and the experiment is visible. We interpret it by a very large uncertainty of the experimental points in this range. This is due to two reasons. First, in this case Ω_1 is divided by very small values of U_1. Actually, in Fig. 9 the uncertainty of the experimental points increases rapidly for decreasing θ. Second, for small angles the light reflections from the fixed sphere cause a systematic error of the order of one and two pixels in the determination of the positions (cf. Figs. 6 and 10).

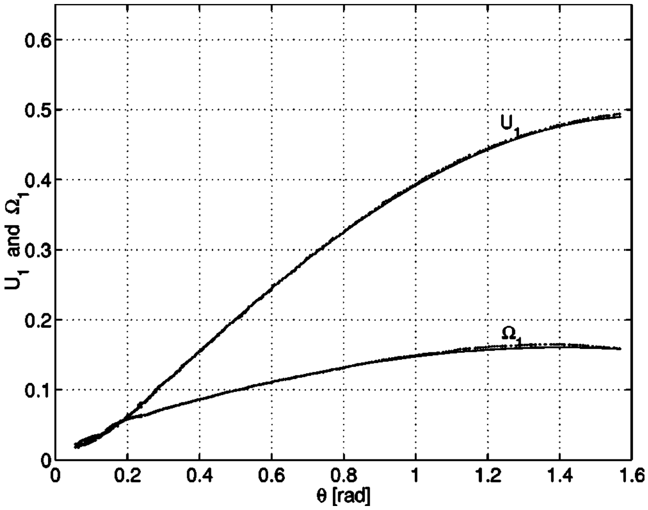

FIG. 8. Angular and translational velocities (in the Stokes units). Dots: numerical derivatives of the experimental data; solid lines: theoretical relation (pure rolling for $\theta<\theta_s$ and rolling with slip for $\theta>\theta_s$); $\mu_k=0.115$, $\xi=0.003$, $v_0=0.83$, $\theta_s=0.20$.

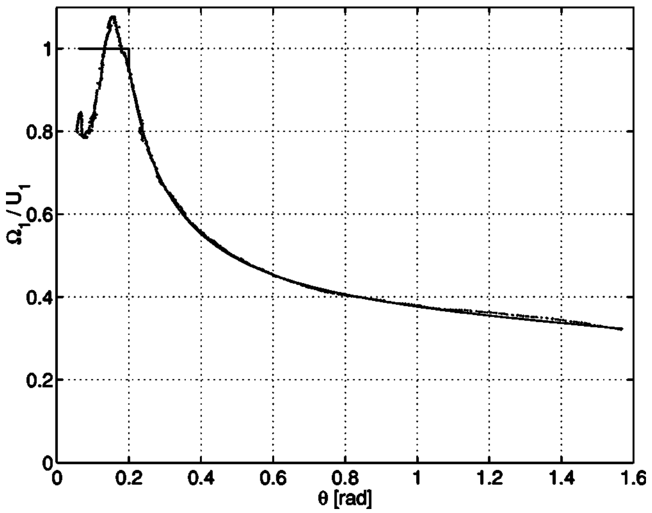

FIG. 9. The ratio of the angular and translational velocities (measured in the Stokes units). Dots: numerical derivative of the experimental data; solid lines: theoretical relation (pure rolling for $\theta<\theta_s$ and rolling with slip for $\theta>\theta_s$); $\mu_k=0.115$, $\xi=0.003$, $v_0=0.83$, $\theta_s=0.20$.

The translational velocities evaluated from the video measurements can be now compared with the previous results obtained by the interferometric method [15]. In Fig. 10 we plot the video data in the same way as the interferometric data were plotted in Fig. 10 of Ref. [15]. In both cases, a change of the slope, interpreted as the transition from pure rolling to rolling with slip, is observed.

Finally, let us compare the estimation of the effective distance between the sphere surfaces ξ obtained in this work with the previous estimation for the same system [15]. The interferometric measurements of the translational motion in Ref. [15] gave $\xi=3\times10^{-5}-3\times10^{-3}$ (i.e., $\xi a=0.1\ \mu\mathrm{m}-10\ \mu\mathrm{m}$). However, these limits followed from the imposed requirement that the effective Stokes velocity (in the closed container) does not exceed the Stokes velocity and the effective distance is not larger than the height of the largest asperities. Now the simultaneous video detection of both rotation and translation allows to estimate ξ *by the fitting procedure* (the results are given in Table I). That is, we significantly improve on accuracy, and therefore we also perform a more rigorous experimental test of validity of the model. The effective distance between the surfaces, ξ, following from the fitting procedure is of the order of the maximal height of asperities on the fixed sphere, that is of the order of 0.003. However, values of ξ given in Table I change from trial to trial. The mean value of $\log_{10}\xi$ for a given trial corresponds to ξ between 0.0023 and 0.0070. The admissible dispersion of $\log_{10}\xi$ for a given trial is 0.23–0.68. The total range of values for all the trials is given as $0.0013\leqslant\xi\leqslant0.0117$. We assign these differences to the experimental error bars. However, a change of roughness from trial to trial cannot be excluded.

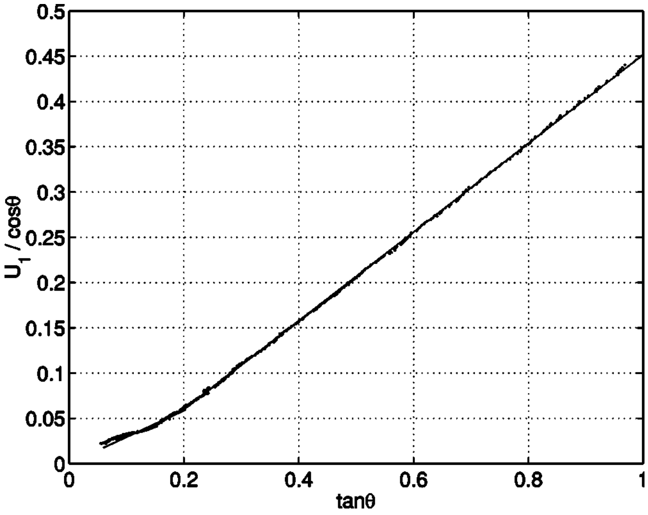

FIG. 10. The translational motion. The dots: the video measurements; the solid straight lines: the model of the contact with $\mu_k = 0.115$, $\xi = 0.003$, $v_0 = 0.83$, $\theta_s = 0.20$. For rolling with slip, the slope is larger than for pure rolling.

VII. CONCLUSIONS

The model of combined hydrodynamic, gravitational, and contact interactions from Ref. [15] was developed to describe the *rotational* motion of a sphere in contact with another fixed sphere, both being immersed in a low-Reynolds-number fluid flow. A video measurement of rotation and translation was performed in addition to the interferometric measurement of translation. A systematic procedure to compare the model and the experiment was designed. The model of contact interactions between the spheres was confirmed, and its parameters determined more precisely than in Ref. [15], where only the translational motion had been investigated.

ACKNOWLEDGMENTS

We are grateful to E. Wajnryb for using his FORTRAN program, which evaluates the two-particle friction matrix. We thank H. Kordoghli and T. Pastureaud for a challenging preliminary study of the problem presented in this paper, done as their training program at ESPCI [53]. We benefited from M. Fermigier's expertise on video systems and from discussions with Y. Peysson, E. Guazzelli, C. Petipas, and K. Masmoudi. The work of M.E.-J. was supported by the Polish KBN through Grant No. 7 T07A 033 18. We also acknowledge funding of our research visits by the CNRS-PAN through Grant No. 2727 and the AMIF grant.

APPENDIX A: THE LUBRICATION EXPRESSIONS FOR TWO-SPHERE HYDRODYNAMIC INTERACTIONS

In Fig. 11 we present functions d,e,r,s,t, which have been used in this work to describe the hydrodynamic interactions between two close spheres.

For small separations between the particle surfaces, i.e., for $\xi \ll 1$, the lubrication asymptotic expansion may be applied to evaluate the two-sphere friction matrix components, Y_{11}^A, Y_{11}^B and Y_{11}^C [1,10],

$$Y_{11}^A = -\frac{1}{6}\ln\xi + 0.9983, \tag{A1}$$

$$Y_{11}^B = \frac{1}{4}\ln\xi + 0.2390 + \frac{1}{8}\xi\ln\xi, \tag{A2}$$

$$Y_{11}^C = -\frac{1}{5}\ln\xi + 0.7028 - \frac{47}{250}\xi\ln\xi. \tag{A3}$$

To test if this approximation is justified for the considered system, we evaluated the exact numerical values of d,e,r,s,t with the use of the numerical program of E. Wajnryb [21] (based on the algorithm from Ref. [8]) and we plotted them together with the corresponding lubrication asymptotic approximation in Fig. 11. For $\xi \leqslant 10^{-2}$ the difference between the exact numerical values of d,e,r,s,t and their lubrication asymptotic approximation does not exceed 0.4% for e, and 0.07% for the other functions. Therefore in Fig. 11 both curves are practically superimposed and the lubrication expansion (A1)–(A3) is sufficiently accurate to describe the motion at contact. This approximation has been used in the numerical fitting procedures, which have been applied in this paper.

APPENDIX B: A SPHERE ROLLING ALONG AN INCLINED PLANE IN VISCOUS FLUID

The goal of this section is to compare the translational and angular velocities of a sphere close to the motionless sphere of equal radius with the corresponding velocities of the same sphere close to a motionless rigid plane. The plane can be

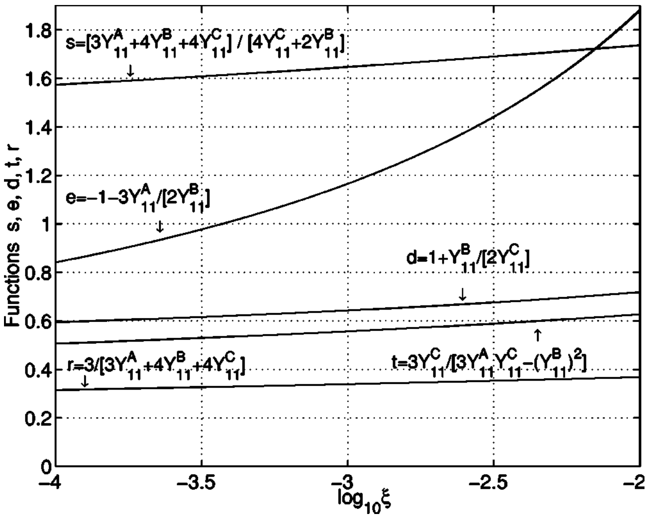

FIG. 11. The functions d,e,r,s,t, introduced in Eqs. (5) and (10)–(12), are given in terms of Y_{11}^A, Y_{11}^B, and Y_{11}^C, the components of the friction matrix ζ_{11} [1,10]. Note that d,e,r,s,t depend on ξ logarithmically and therefore they change only a little in a wide range of ξ.

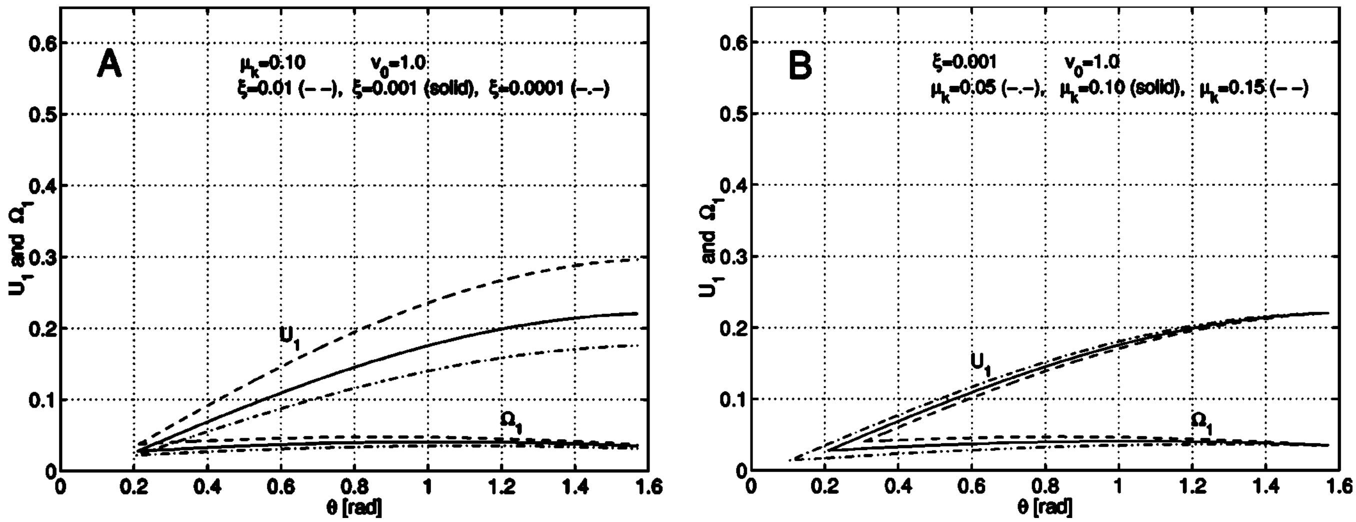

FIG. 12. The translational and angular velocities (normalized by v_{st} and v_{st}/a, respectively) of a sphere rolling with slip along an inclined plane (theoretical results).

interpreted as "a sphere of an infinite radius," therefore the comparison gives also some idea about the change in the relative motion of the two spheres with the ratio of their radii.

The translational and rotational motion of a sphere in contact with an inclined plane is calculated from the same model of mechanical friction as for the two spheres, replacing the lubrication asymptotic expressions for two spheres (Appendix A) by the corresponding formulas for a sphere and a plane [54,55].

We plot the results for the rolling-with slip of a sphere along an inclined plane in Figs. 12 and 13, using the same values of the gap size ξ and kinetic friction coefficient μ_k as the ones applied in Figs. 3 and 4 for the two spheres.

By comparison of Figs. 3(a) and 3(b) with Figs. 12(a) and 12(b), respectively, one can see essentially the same dependence of the angular and translational velocities on the inclination angle θ, and a similar sensitivity to a change of μ_k and ξ. However, the velocities are significantly smaller for a plane than for a fixed sphere.

By comparison of Figs. 4(a) and 4(b) with Figs. 13(a) and 13(b), respectively, one can observe a similar sensitivity of the angular and translational velocity ratio to a change of μ_k and ξ. The contribution to the overall motion coming from the rotation is larger for a fixed sphere than for a plane, especially for larger angles θ.

The same expressions for the rolling with slip of a sphere along an inclined plane were given earlier in Ref. [41], together with the experimental data. Note that the quantities plotted in Fig. 3(a) and Fig. 4(a) from Ref. [41] are $U_1/\sin\theta$ and $\Omega_1/\sin\theta$ rather than U_1 and Ω_1, plotted in Fig. 12. Moreover, Figs. 4(a) and 4(b) from Ref. [41] need to be corrected according to the theoretical expressions from Refs. [54–56].

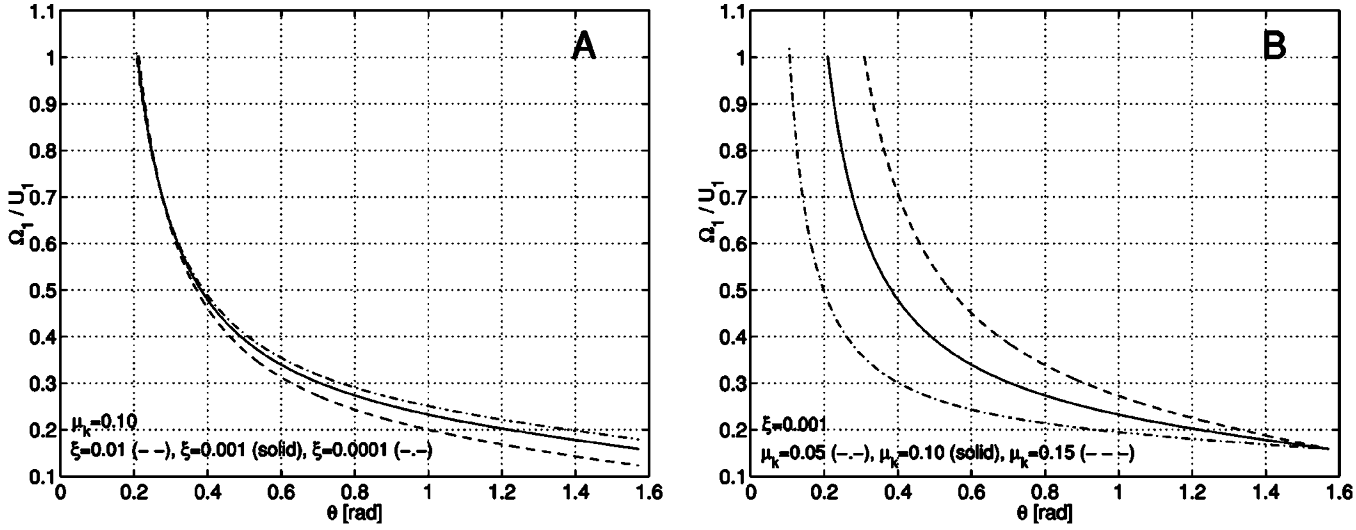

FIG. 13. The ratio of the angular and translational velocities of a sphere rolling with slip along an inclined plane (theoretical results).

[1] S. Kim and S.J. Karrila, *Microhydrodynamics: Principles and Selected Applications* (Butterworth-Heinemann, Boston, 1991).

[2] G.K. Batchelor, J. Fluid Mech. **52**, 245 (1972).

[3] G.K. Batchelor and J.T. Green, J. Fluid Mech. **56**, 401 (1972).

[4] P. Mazur, Helv. Phys. Acta **59**, 263 (1986).

[5] P. Mazur, Faraday Discuss. Chem. Soc. **83**, 33 (1987).

[6] B.U. Felderhof, Physica A **151**, 1 (1988); in *Fundamental Problems in Statistical Mechanics VII*, edited by H. van Beijeren (North-Holland, Amsterdam, 1990).

[7] J. Happel, H. Brenner, *Low Reynolds Number Hydrodynamics* (Noordhoff, Leiden, 1991).

[8] B. Cichocki, B.U. Felderhof, R. Schmitz, PCH, PhysicoChem. Hydrodyn. **10**, 383 (1988).

[9] B. Cichocki, in *Continuum Models and Discrete Systems*, edited by K. Z. Markov (World Scientific, Singapore, 1996).

[10] D.J. Jeffrey and Y. Onishi, J. Fluid Mech. **139**, 261 (1984).

[11] P.A. Arp and S.G. Mason, J. Colloid Interface Sci. **61**, 21 (1977); **61**, 44 (1977).

[12] L.A. Mondy, A.L. Graham, P. Stroeve, and A. Majumdar, AIChE J. **33**, 862 (1987).

[13] R.H. Davis, Phys. Fluids A **4**, 2607 (1992).

[14] S. Zeng, E.T. Kerns, and R.H. Davis, Phys. Fluids **8**, 1389 (1996).

[15] M.L. Ekiel-Jeżewska, F. Feuillebois, N. Lecoq, K. Masmoudi, R. Anthore, F. Bostel, and E. Wajnryb, Phys. Rev. E **59**, 3182 (1999).

[16] M.P. Petrich and D.L. Koch, Phys. Fluids **10**, 2111 (1998).

[17] K.P. Galvin, Y. Zhao, and R.H. Davis, Phys. Fluids **13**, 3108 (2001).

[18] G. Bossis and J.F. Brady, J. Chem. Phys. **80**, 5141 (1984).

[19] A.J.C. Ladd, J. Chem. Phys. **88**, 5051 (1988); **90**, 1149 (1989); **93**, 3484 (1990).

[20] A.S. Sangani and G. Mo, Phys. Fluids **6**, 1653 (1994).

[21] B. Cichocki, M.L. Ekiel-Jeżewska, and E. Wajnryb, J. Chem. Phys. **111**, 3265 (1999).

[22] B. Cichocki, M.L. Ekiel-Jeżewska, P. Szymczak, and E. Wajnryb, J. Chem. Phys. **117**, 1231 (2002).

[23] For example, the numerical algorithms from Refs. [21,22] may be generalized to evaluate the influence of the contact interactions on a modification of the three-particle contribution to the self-diffusion and to the suspension sedimentation velocity.

[24] F.R. da Cunha and E.J. Hinch, J. Fluid Mech. **309**, 211 (1996).

[25] I. Rampall, J.R. Smart, and D.T. Leighton, J. Fluid Mech. **339**, 1 (1997).

[26] R.R. Sundarajakumar and D.L. Koch, J. Non-Newtonian Fluid Mech. **73**, 205 (1997).

[27] H.J. Wilson and R.H. Davis, J. Fluid Mech. **421**, 339 (2000).

[28] H.J. Wilson and R.H. Davis, J. Fluid Mech. **452**, 425 (2002).

[29] M. Tabatabaian and R.G. Cox, Int. J. Multiphase Flow **17**, 395 (1991).

[30] A. Nir and A. Acrivos, J. Fluid Mech. **59**, 209 (1973).

[31] S. Wakiya, J. Phys. Soc. Jpn. **31**, 1581 (1971).

[32] F. P. Bowden and D. Tabor, *The Friction and Lubrication of Solids* (Clarendon, Oxford, 1950).

[33] S. H. Crandall, N. C. Dahl, and T. J. Lardner, *An Introduction to the Mechanics of Solids* (McGraw-Hill, New York, 1978).

[34] K. L. Johnson, *Contact Mechanics* (Cambridge University Press, Cambridge, 1985).

[35] K. Masmoudi, N. Lecoq, R. Anthore, F. Bostel, and F. Feuillebois, Exp. Fluids **32**, 55 (2002).

[36] N. Lecoq, F. Feuillebois, N. Anthore, R. Anthore, F. Bostel, and C. Petipas, Phys. Fluids A **5**, 3 (1993).

[37] K. Masmoudi, Ph. D. thesis, Université de Rouen, 1998.

[38] When this manuscript was under review, we learned about another paper [57], in which the relative rotational motion of two sedimenting spheres had been analyzed theoretically and experimentally.

[39] Note that $\boldsymbol{\zeta}_{11}^{-1}$ is not equal to the mobility matrix $\boldsymbol{\mu}_{11}$ defined in Refs. [6,10].

[40] M. L. Ekiel-Jeżewska, N. Lecoq, R. Anthore, F. Bostel, F. Feuillebois, in *Tubes, Sheets and Singularities in Fluid Dynamics*, edited by K. Bajer and H. K. Moffatt (Kluwer Academic Dordrecht, 2002), p. 343.

[41] J.R. Smart, S. Beimfohr, and D.T. Leighton, Phys. Fluids A **5**, 13 (1993).

[42] J.R. Smart and D.T. Leighton, Jr., Phys. Fluids A **1**, 52 (1989).

[43] G.I. Taylor, J. Fluid Mech. **49**, 319 (1971).

[44] S. Richardson, J. Fluid Mech. **76**, 827 (1976).

[45] L.M. Hocking, J. Fluid Mech. **76**, 801 (1976).

[46] M.E. O'Neill and S.R. Majumdar, Z. Angew. Math. Phys. **21**, 180 (1970).

[47] D.J. Jeffrey and Y. Onishi, Z. Angew. Math. Phys. **35**, 634 (1984).

[48] N. Lecoq, F. Feuillebois, R. Anthore, C. Petipas, and F. Bostel, J. Phys. II **5**, 323 (1995).

[49] H. Brenner, Chem. Eng. Sci. **16**, 242 (1961).

[50] A.D. Maude, Br. J. Appl. Phys. **12**, 293 (1961).

[51] W. H. Press, S. A. Teukolsky, W. T. Vetterling, and B. P. Flannery, *Numerical Recipes* (Cambridge University Press, Cambridge, 1992).

[52] The accuracy of the numerical derivative is higher than the difference between the experimental and theoretical points in Figs. 8 and 9. A change for $K=200$ or $K=300$ results in a shift of the points in Figs. 8 and 9, which is of the order of the maximal difference between the experiment and the model in Fig. 8, and in Fig. 9 for $\theta>0.2$. The numerical derivatives with $L=3$ and $L=4$ are practically the same.

[53] T. Pastureaud and H. Kordoghli, report, 1998 (unpublished).

[54] M.E. O'Neill and K. Stewartson, J. Fluid Mech. **27**, 705 (1967).

[55] A.J. Goldman, R.G. Cox, and H. Brenner, Chem. Eng. Sci. **22**, 637 (1967).

[56] B. Cichocki and R.B. Jones, Physica A **258**, 273 (1998).

[57] Y. Zhao and R.H. Davis, Chem. Eng. Sci. **57**, 1997 (2002).